*Astronomy & Astrophysics* manuscript no. paper
February 27, 2026




# Little red dots as obscured little blue dots: a super-Eddington unification model

Piero Madau[1,2] and Roberto Maiolino[3,4,5]

[1] Dipartimento di Fisica "G. Occhialini," Università degli Studi di Milano-Bicocca, Piazza della Scienza 3, I-20126 Milano, Italy
[2] Department of Astronomy & Astrophysics, University of California, 1156 High Street, Santa Cruz, CA 95064, USA
[3] Kavli Institute for Cosmology, University of Cambridge, Madingley Road, Cambridge CB3 0HA, UK
[4] Cavendish Laboratory, University of Cambridge, 19 JJ Thomson Avenue, Cambridge CB3 0HE, UK
[5] Department of Physics and Astronomy, University College London, Gower Street, London WC1E 6BT, UK

February 27, 2026

**ABSTRACT**

We investigate whether Little Red Dots (LRDs) are the dust-reddened, high-inclination counterparts of compact, blue broad-line AGNs ("Little Blue Dots", LBDs) powered by super-Eddington accretion. We model the central engine as a geometrically thick, radiation–pressure supported accretion flow whose funnel produces strongly anisotropic, intrinsically blue ionizing continua, coupled to an equatorially concentrated broad-line region (BLR) and a dusty reprocessing screen with modest covering factor. Using inclination-dependent spectral energy distributions (SEDs) as input to Cloudy, we show that the extreme broad H$\alpha$ equivalent widths (EWs) of JWST LRDs can be reproduced with global BLR covering factors of only $C_{\rm BLR} \simeq 0.15$, fully consistent with standard Type 1 AGNs and far below unity. Large Balmer EWs arise because self-shadowing suppresses the high-inclination optical continuum while the BLR is illuminated by an ionizing-rich EUV SED. Weak high-ionization lines (e.g. HeII $\lambda$4686) follow from the orientation-dependent suppression of the XUV/soft X-ray continuum toward equatorial directions, without requiring a fully enclosing gaseous "cocoon". Applying a gray dust attenuation law with $A_V \simeq 2.8$ along high-inclination (LRD-selected) sightlines, our fiducial model reproduces the V-shaped UV-optical continua of LRDs and the large Balmer decrements; strong Balmer breaks arise only along the most obscured sightlines. A compact equatorial dust structure with modest global covering factor tied to the BLR, normalized by energy conservation, intercepts and reradiates only a small fraction of the bolometric luminosity, yielding a modest hot-dust bump and far-IR/sub-mm output consistent with current measurements and limits and implying small dust masses. This single-framework model links LRD and LBD observables through orientation, predicting correlated trends in H$\alpha$ EW, Balmer decrement, Balmer break, high-ionization line strengths, and IR emission.

**Key words.** Accretion (14); Active galactic nuclei (16); James Webb Space Telescope (2291); Supermassive black holes (1663)

## 1. Introduction

The James Webb Space Telescope (JWST) has uncovered a rich population of moderate-luminosity broad-line active galactic nuclei (BLAGNs) at $z \gtrsim 4$, powered by accretion onto early massive black holes (MBHs) with inferred masses $\sim 10^6$–$10^8\,M_\odot$ (e.g., Harikane et al. 2023; Maiolino et al. 2024; Taylor et al. 2025; Juodžbalis et al. 2025a). These sources appear to outnumber the extrapolation of the quasar population at low luminosities by orders of magnitude, and constraints from existing multiwavelength data – in particular deep X-ray imaging and stacking analyses – indicate that many are unusually weak in X-rays compared to low-redshift Type 1 AGNs (e.g., Ananna et al. 2024; Yue et al. 2024; Maiolino et al. 2025). Their space density, spectral shapes, and weak high-energy emission challenge standard inferences about MBH growth, accretion physics, and AGN selection in the first few Gyrs after the Big Bang.

A striking empirical aspect of this JWST BLAGN census is their compactness: many appear as unresolved or barely resolved "little dots" in rest-frame optical imaging. Recent work has proposed a useful shorthand that partitions these compact JWST BLAGNs by their UV-optical continuum slopes into "Little Red Dots" (LRDs) and "Little Blue Dots" (LBDs), with LRDs denoting the red rest-optical, V-shaped minority subset and LBDs the comparably compact, bluer-continuum majority (Brazzini et al. 2026). In JADES, LRD-like objects comprise ∼10%–30% of the BLAGN sample, with the inferred fraction decreasing toward lower bolometric luminosities (Hainline et al. 2025).

LRDs are commonly identified as sources with a V-shaped UV-optical SED in which the continuum turns sharply at $\lambda_{\rm rest} \sim 0.35$–$0.40\,\mu$m, near the Balmer limit (e.g., Matthee et al. 2024; Greene et al. 2024; Kocevski et al. 2025; Wang et al. 2025; Hainline et al. 2025; Akins et al. 2025b; Delvecchio et al. 2025; Barro et al. 2025). Homogeneous spectroscopy has clarified that the LRD phenomenology is not defined by color alone: objects exhibiting a V-shaped continuum are strongly associated with broad Balmer emission and with a dominant unresolved component in the rest-frame optical (Hviding et al. 2025). This

empirical triad – V-shaped UV-optical continuum, broad Balmer lines, and a rest-optical point-source component – suggests that the central engine contributes substantially to the observed light, even when broadband colors might otherwise encourage a stellar interpretation. Several of these characteristics – enhanced Balmer emission, weak high-ionization features, and weak or absent X-rays – extend into the broader BLAGN population, with LRDs occupying the most extreme tail (Hviding et al. 2025).

A key clue is that these JWST BLAGNs are extreme Balmer emitters while simultaneously showing weak high-ionization rest-UV features. In the RUBIES census, LRDs occupy a particularly extreme locus in the $L_{\mathrm{H}\alpha}$–$M_{\mathrm{UV}}$ plane: while LRDs are faint in the rest-UV at fixed $L_{\mathrm{H}\alpha}$, the most extreme H$\alpha$ emitters are dominated by LRDs, i.e. LRDs constitute the most luminous H$\alpha$ emitters at fixed UV luminosity (Hviding et al. 2025). Consistent with this, the median rest-frame EW reported for the broad H$\alpha$ line in JWST-identified $z > 4$ BLAGNs is $\simeq 570$ Å, roughly a factor of $\sim 3$ higher than in typical low-$z$ AGNs (Maiolino et al. 2025), while in the LRDs subpopulation the H$\alpha$ EW is even higher (de Graaff et al. 2025). Yet high-ionization rest-UV lines such as CIV, HeII, and NV are frequently weak or undetected in BLAGNs with rest-UV coverage, including the LRD subset (e.g., Lambrides et al. 2024; Tang et al. 2025; Juodžbalis et al. 2025a; Zucchi et al. 2025). The joint occurrence of extreme Balmer emission and suppressed high-ionization lines places strong constraints on the ionizing SED incident on the BLR and on the geometry and obscuration of the line-emitting region. In anisotropic-emission geometries where the observer receives a continuum boosted relative to the radiation intercepted by the BLR, recombination-line EWs are expected to be reduced, making H$\alpha$ an orientation-sensitive diagnostic (e.g., Madau 2025).

Although the origin of the LRD continuum remains debated, the spectroscopic and morphological evidence motivates an AGN-dominated interpretation for at least a substantial fraction of the population. Motivated by the emerging LBD/LRD taxonomy, we consider an orientation-obscuration continuity picture in which LRDs are not a separate class of engines, but rather represent LBD-like BLAGNs viewed through substantial circumnuclear dust and gas. In this view, LRDs and LBDs share a common engine, with both classes potentially subject to some host-galaxy reddening, while the V-shaped SED and red rest-optical slope of LRDs arise from additional circumnuclear attenuation and reprocessing along higher-inclination sightlines. Such a geometry naturally connects compactness, optical redness, weak variability, and suppressed X-rays to line-of-sight processing, while allowing broad lines to remain visible.

A natural physical framework that can supply both strong anisotropy and self-occultation is rapid accretion in the super-Eddington regime. Geometrically thick flows with funnel-like structures produce strong inclination-dependent SEDs and self-shadowing, which can reshape the UV-optical continuum and modulate the illumination of the BLR (Wang et al. 2014; Lupi et al. 2024; Madau 2025). In addition, X-ray emission can be intrinsically weak if a hot corona is efficiently Compton-cooled by the intense soft-photon field in the inner flow, suppressing hard X-rays even before line-of-sight obscuration is considered (Madau & Haardt 2024). Here, we investigate whether the combination of dense BLR gas, anisotropic emission from super-Eddington accretion, and dust reddening can provide a coherent framework for the defining features of LRDs – their V-shaped UV-optical continua, extreme Balmer emission (including large H$\alpha$ equivalent widths), weak high-ionization lines, and suppressed variability – and we assess how LRDs relate to the broader population of JWST-discovered high-redshift BLAGNs, including the putative LBD majority.

## 2. Super-Eddington accretion

We model the engines of JWST BLAGNs at $z > 4$ as geometrically thick, moderately super-Eddington accretion flows with rates $\dot{m} \simeq 10$–$30$, where $\dot{m} \equiv \dot{M}/\dot{M}_{\mathrm{Edd}}$ and $\dot{M}_{\mathrm{Edd}} \equiv 10\, L_{\mathrm{Edd}}/c^2$. For these accretion rates, the corresponding Eddington ratio is $\lambda_{\mathrm{Edd}} \equiv L_{\mathrm{bol}}/L_{\mathrm{Edd}} \simeq 4$–$7$, reflecting the decline of the effective radiative efficiency at increasing $\dot{m}$ in thick-disk solutions, where the inner edge (cusp) shifts inward toward the marginally bound orbit, reducing the binding energy released as radiation. We adopt the non-advective, radiation-pressure supported torus formalism in which the disk surface follows equipotential contours set by an assumed specific-angular-momentum distribution (Paczyński & Wiita 1980). On the photosphere, hydrostatic balance requires that the net outward radiative flux, $F_{\mathrm{net}} = F_{\mathrm{out}} - F_{\mathrm{in}}$, balances the local effective gravity (e.g., Sikora 1981; Madau 1988). Because the funnel walls are mutually visible, nonlocal self-irradiation implies $F_{\mathrm{in}} \neq 0$. In the idealized perfect-reflection limit used here, incident radiation is re-emitted without thermalization, so the local temperature is set by the locally generated flux while the outward flux $F_{\mathrm{out}}$ can be enhanced by reflected/scattered contributions. The resulting "mirror" funnel naturally yields self-consistent super-Eddington thick-disk geometries with strong collimation toward the rotation axis and self-shadowing at high inclinations.

Global MHD and radiation-GRMHD simulations of mildly supercritical accretion broadly support this qualitative picture, producing radiation-pressure supported inner tori, equatorial outflows, and a narrow funnel-shaped photosphere that channels escaping radiation toward the symmetry axis (e.g., Jiang et al. 2014; Pacucci & Narayan 2024; Zhang et al. 2025).

### 2.1. Anisotropic intrinsically blue SEDs

Following Madau (2025), we compute inclination-dependent, scattering-modified blackbody SEDs for a fiducial $M_{\mathrm{BH}} = 10^{7.5}\, M_{\odot}$ accretor at $\dot{m} \simeq 32$. The key outcome is a strongly anisotropic ionizing continuum: the EUV/soft-X photon output is highest for near-polar sightlines and is rapidly suppressed toward edge-on views by geometric foreshortening and self-shadowing, while the UV-optical continuum varies much more weakly with inclination. In the remainder of the paper we therefore characterize orientation-dependent "hardness" using photon-rate ratios above selected ionization thresholds (Fig. 1), which directly track the supply of H- and He-ionizing photons and the availability of the hardest EUV photons relevant for high-ionization species.

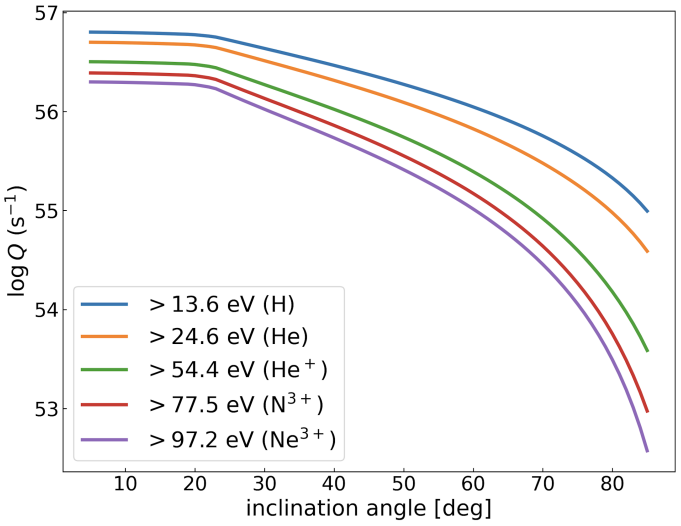


**Fig. 1.** Angle-dependent ionizing photon production rates, $Q(>E_{\rm th})$, for a super-Eddington accretion flow with $M_{\rm BH} = 10^{7.5}\,M_\odot$ and $\dot{m} = 32$ (Model A of Madau 2025). The curves show the integrated photon rate ($\rm s^{-1}$) above five ionization thresholds: HI (13.6 eV), HeI (24.6 eV), HeII (54.4 eV), NIV (77.5 eV), and NeIV (97.2 eV). The rates are strongly anisotropic, remaining near their peak values for $i \lesssim 25^\circ$ but declining steeply at high inclinations as self-shadowing obscures the hot inner funnel and the emergent spectrum becomes dominated by the cooler outer disk. From face-on to edge-on, the highest-threshold photon rates decrease by $\gtrsim$2–3 dex.

We note that these models can produce a very blue rest-UV continuum, comparable to – and in some cases steeper than – the standard thin-disk asymptotic slope $f_\lambda \propto \lambda^{-7/3}$ ($\beta = -2.33$). In the $(\beta_{\rm UV}, \beta_{\rm opt})$ plane, several JWST LBDs extend to very blue continua, approaching the slopes expected for an unreddened accretion disk (Hainline et al. 2025; Brazzini et al. 2026). Interestingly, fitting the NIRSpec optical continuum of the Red Rosetta Stone GN–28074 with a dust-absorbed power-law, Brazzini et al. (2026) infer an intrinsic slope $\beta = -2.49 \pm 0.15$, i.e. close to accretion disk expectations.

### 2.2. Accretion flow geometry and the BLR

We adopt a simple equatorial BLR geometry motivated by reverberation-mapping constraints (e.g., Du et al. 2025; Pozo Nuñez et al. 2014) and microlensing distortions of broad-line profiles (e.g., Hutsemékers et al. 2023; Savić et al. 2024; Gaskell 2009). In the present implementation, the BLR is represented as a clumpy, equatorially concentrated distribution whose line-of-sight obscuration is described probabilistically by an inclination-dependent escape probability $P(i)$ (see below). We compute the incident radiation field using the SED evaluated at $i = 80^\circ$, which corresponds to a representative (solid-angle median) viewing angle for the equatorial cloud population.

In super-Eddington funnel geometries, gas near the equatorial plane is illuminated by a softer, self-shielded ionizing continuum than that seen along polar lines of sight, naturally suppressing high-ionization emission while preserving strong Balmer recombination lines. Our baseline BLAGN geometry is depicted in Figure 2 and includes an inner, geometrically thick torus extending to $r_{\rm out} \simeq 1000\,r_{\rm S}$. The BLR is assumed to reside at much larger radii in an equatorial distribution, with its outer portion beyond the sublimation radius embedded in (or contiguous with) a dusty circumnuclear torus (see below). To extend the SED beyond the outer edge of the supercritical funnel, we match the thick-disk solution to a standard radiation-pressure dominated thin disk by setting a transition radius $r_t = 0.93\,r_{\rm out}$ and enforcing continuity of the effective temperature and radiative flux at $r_t$; outside $r_t$ the thin-disk flux follows the standard Keplerian scaling $F(r) \propto r^{-3}$ and is intrinsically subdominant in the UV. We truncate the outer disk at $r = 1500\,r_{\rm S}$ near the expected self-gravity radius.

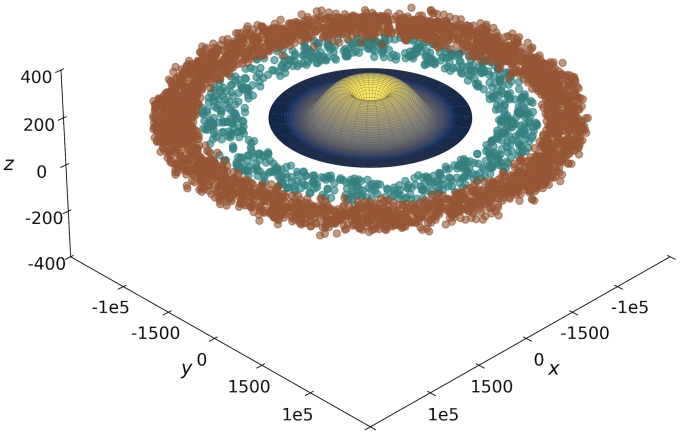


**Fig. 2.** Three-dimensional toroidal geometry of a super-Eddington BLAGN accreting at $\dot{m} = 32$, viewed at an inclination angle of $i = 60^\circ$. The spatial coordinates $x, y$, and $z$ are expressed in units of Schwarzschild radii $r_S$. The thick torus extends out to $\simeq 1000\,r_S$, where it is matched to an outer geometrically thin disk (only shown to $r = 1500\,r_S$ to illustrate the geometric transition). Brighter (yellow) colors indicate higher surface brightness, while darker (blue) colors indicate lower values. The teal spheres provide a schematic (not-to-scale) visualization of BLR clouds; physically, the BLR lies at much larger radii ($\sim 10^5\,r_S$), and its outer portion beyond the sublimation radius is expected to be dusty. The outer brown structure schematically represents a dusty circumnuclear obscurer (a torus-like structure) surrounding the BLR.

## 3. Extreme Hα EWs: blue SEDs vs. covering factor

The extreme Balmer-line strengths of LRDs (Hviding et al. 2025) motivate a direct test of whether their large Hα EWs are compatible with standard BLR covering factors given the ionizing SEDs predicted by our super-Eddington models. We generated grids of photoionization models with the C23 release of CLOUDY (Chatzikos et al. 2023), tailored to typical BLR conditions ($n_{\rm H} = 10^{10}\,\rm cm^{-3}$, $N_{\rm H} = 10^{23}\,\rm cm^{-2}$). We varied the ionization parameter $U$ and adopted a metallicity representative of galaxies at the redshifts where LRDs and LBDs are most commonly found, $Z = 0.1\,Z_\odot$. Predicted line strengths were compared to LRD observations (analogous to the LBD comparison in Madau 2025). To translate CLOUDY outputs into observables, we normalized the global BLR covering factor, $C_{\rm BLR}$,

by scaling our fiducial model to match the median EW of 570 Å reported by Maiolino et al. (2025).

For each observer inclination $i$, we compute the rest-frame EW of a line at wavelength $\lambda_0$ as

$$\mathrm{EW}(i) = \frac{F_{\mathrm{line}}(i_{\mathrm{BLR}})}{F_{\lambda,\mathrm{cont}}(\lambda_0; i)}. \tag{1}$$

In the present implementation, the BLR line emission is computed with CLOUDY for an incident continuum corresponding to a representative BLR inclination $i_{\mathrm{BLR}} = 85°$. Hence $F_{\mathrm{line}}$ depends on $i_{\mathrm{BLR}}$ but is independent of the observer's $i$. The transmitted nuclear continuum through the BLR gas is likewise taken from the same representative CLOUDY run. The continuum flux density per unit wavelength at the line, $F_{\lambda,\mathrm{cont}}(\lambda_0; i)$, is obtained from the observed continuum spectrum as

$$F_{\lambda,\mathrm{cont}}(\lambda; i) = P_{\mathrm{esc}}(i)\, F_{\lambda,\mathrm{disk}}(\lambda; i) + \big[1 - P_{\mathrm{esc}}(i)\big]\, F_{\lambda,\mathrm{tran}}(\lambda; i_{\mathrm{BLR}}) + C_{\mathrm{BLR}}\, F_{\lambda,\mathrm{neb}}(\lambda; i_{\mathrm{BLR}}), \tag{2}$$

evaluated at $\lambda = \lambda_0$. Here $F_{\lambda,\mathrm{disk}}(\lambda; i)$ is the direct, inclination-dependent disk continuum from the accretion flow, $F_{\lambda,\mathrm{tran}}(\lambda; i_{\mathrm{BLR}})$ is the CLOUDY transmitted continuum through the BLR gas (i.e. the incident nuclear continuum after absorption) computed for a representative BLR illumination angle $i_{\mathrm{BLR}}$, and $F_{\lambda,\mathrm{neb}}(\lambda; i_{\mathrm{BLR}})$ is the outward diffuse (nebular) continuum emitted by the BLR in the same CLOUDY calculation. The latter is assumed isotropic and scaled by the global BLR covering factor $C_{\mathrm{BLR}}$. The direct versus transmitted nuclear continuum is weighted by the line-of-sight escape probability $P_{\mathrm{esc}}(i)$, while $C_{\mathrm{BLR}}$ sets the amplitude of the BLR reprocessed emission.

We model the BLR as a clumpy, equator-concentrated cloud distribution by specifying the mean number of clouds intersected along a line of sight at inclination $i$ as

$$N_{\mathrm{los}}(i) = N_0 \exp\left[-\frac{\cos^2 i}{2\sigma_c^2}\right], \tag{3}$$

(see, e.g., the formalism of Nenkova et al. 2008), where $\sigma_c$ controls the angular thickness of the cloud distribution about the equatorial plane. The corresponding escape probability for direct disk photons is

$$P_{\mathrm{esc}}(i) = \exp\big[-N_{\mathrm{los}}(i)\big]. \tag{4}$$

We fix the normalization $N_0$ by requiring that the angle-averaged probability of intercepting at least one cloud equals the global covering factor,

$$C_{\mathrm{BLR}} = \int_0^{\pi/2} \big[1 - P_{\mathrm{esc}}(i)\big] \sin i \, \mathrm{d}i, \tag{5}$$

where we have used symmetry about the mid-plane. In practice, for a chosen $\sigma_c$ we solve equation (5) for $N_0$. For $\sigma_c = 0.26$, the distribution is strongly equator-weighted, with a median near 80°, motivating our adoption of $i_{\mathrm{BLR}} = 80°$ for the incident SED in the CLOUDY calculations. Finally, we scale the CLOUDY line output by the global covering factor,

$$F_{\mathrm{line}}(i_{\mathrm{BLR}}) = C_{\mathrm{BLR}}\, f_{\mathrm{line}}(i_{\mathrm{BLR}}), \tag{6}$$

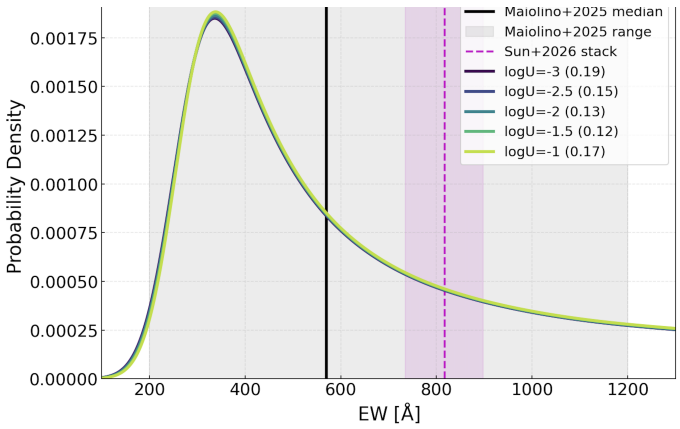


**Fig. 3.** Probability density functions (PDFs) of the broad H$\alpha$ EW predicted by our fiducial super-Eddington accretor with $M_{\mathrm{BH}} = 10^{7.5}\, M_\odot$ and $\dot{m} = 32$. The distributions are derived by weighting the inclination-dependent EWs by the geometric probability $p(i) = \sin i$ ($0 \le i \le \pi/2$), assuming random observer orientations. Different curves correspond to different ionization parameters $\log U$, as indicated in the legend. For each model, the global BLR covering factor $C_{\mathrm{BLR}}$ is scaled such that the probability-weighted median of the theoretical distribution matches the observed median EW of 570 Å from the high-$z$ BLAGN sample of Maiolino et al. (2025) (vertical black line). The resulting required covering factors are listed in parentheses in the legend and are relatively modest ($C_{\mathrm{BLR}} = 0.12$–$0.19$). The gray shaded region denotes the full range of EWs observed in the JADES sample (200–1200 Å). The high-EW tail above 1200 Å corresponds to highly inclined ($i \gtrsim 80°$) observers. Also shown is the total (broad+narrow) EW recently measured from a median-stacked LRD spectrum by Sun et al. (2026) (magenta dashed line with shaded uncertainty band), which lies toward the high-EW (high-inclination) side of the distribution.

where $f_{\mathrm{line}}(i_{\mathrm{BLR}})$ is the line flux predicted by CLOUDY per unit covering for the adopted cloud parameters and incident SED at $i_{\mathrm{BLR}}$.

Figure 3 displays the resulting broad H$\alpha$ EW probability density functions (PDFs), computed assuming random observer orientations weighted by the random-orientation distribution $p(i) = \sin i$. The shaded region indicates the full range of EWs observed in the high-$z$ sample of Maiolino et al. (2025) (200 $\lesssim$ EW $\lesssim$ 1200 Å). While the observed histogram is a population statistic that also reflects intrinsic scatter in black hole mass, accretion rate, and BLR gas properties, our model curves isolate the variance due to orientation alone and are therefore narrower. Nevertheless, the shift of the probability-weighted peak EW with ionization parameter provides a useful handle on the overall scaling needed to reproduce typical line strengths. In the most edge-on tail of the orientation distribution, the model predicts very large EWs because the observed optical continuum decreases approximately geometrically, $\propto \cos i$, while the broad-line luminosity is assumed to be isotropic. In practice, once the direct nuclear continuum becomes extremely faint – in our models this occurs at $i \gtrsim 85°$ – the observed rest-optical continuum will not continue to dim indefinitely. A low-level continuum floor from host starlight and/or scattered AGN light is expected to dominate over the highly foreshortened direct disk emission at these inclinations, effectively truncating the high-EW tail. We therefore impose a conservative cap EW(H$\alpha$) $\le$ 2000 Å when

constructing the PDFs. This cap affects only the extreme edge-on tail and does not alter the probability-weighted median used to calibrate $C_{\rm BLR}$.

Matching the probability-weighted median of the models to the observed median implies global covering factors of $C_{\rm BLR} \simeq 0.12$–$0.19$. These values are consistent with standard estimates for low-$z$ Type 1 AGNs (e.g., Peterson 2006; Pandey et al. 2023). In this framework, $C_{\rm BLR}$ is simply the sky fraction covered by BLR clouds as seen from the central engine, i.e. the angle-averaged probability that an emitted photon encounters at least one cloud. For a clumpy, non-axisymmetric distribution, $C_{\rm BLR}$ is an average over azimuth and polar angle of the cloud covering probability, and does not imply unity covering along any specific subset of sightlines. We note that the EW distribution reported by Maiolino et al. (2025) combines objects spanning the emerging LBD/LRD taxonomy, including JADES sources as well as systems drawn from the literature. In our framework, LBDs and LRDs occupy different parts of this distribution: less-reddened LBDs should preferentially exhibit lower EWs, whereas obscured, high-inclination LRDs should populate the high-EW tail. This prediction is directly testable by measuring EW distributions separately for LBD and LRD subsamples, controlling for luminosity and redshift.

Interestingly, a recent median-stacked LRD spectrum from Sun et al. (2026) yields total (broad+narrow) equivalent widths EW(H$\alpha$) $= 817.2^{+80.9}_{-82.7}$ Å and EW(H$\beta$) $= 109.8^{+6.8}_{-6.9}$ Å. In our inclination-only model, such large Balmer EWs are naturally attained only for highly inclined sightlines. Figure 4 shows that matching the Sun et al. stack requires inclinations $i \gtrsim 65$–$70°$ (depending weakly on $\log U$), with lower-inclination views underpredicting both EW(H$\alpha$) and EW(H$\beta$). This may support the interpretation that color-selected LRDs correspond to the high-inclination tail of the same underlying super-Eddington BLAGN population whose less-reddened, more face-on analogues appear as LBDs. We caution, however, that these stacked measurements correspond to total (broad+narrow) EWs at the PRISM resolution, where a robust decomposition into broad and narrow components is not generally possible; the broad-line EWs relevant for our BLR modeling may therefore be somewhat smaller.

Our results contrast with Yan et al. (2025), who argue that the observed broad H$\alpha$ strengths require near-unity covering factors and therefore invoke an enshrouded geometry with nearly $4\pi$ coverage by dense gas ($n_{\rm H} = 10^8$–$10^{10}\,{\rm cm}^{-3}$). In our super-Eddington models, large Balmer EWs can be produced with modest $C_{\rm BLR}$ because the BLR-illuminating continuum has a higher ionizing-to-optical photon budget than standard quasar composites, and the inclination dependence is driven by anisotropic continuum dilution at fixed line emission. For more face-on sightlines, the observer sees the boosted funnel continuum, whereas the BLR does not intercept a proportionally larger ionizing flux, so the lines are diluted and the EWs fall to values typical of Type 1 AGNs. Thus, the most extreme LRD H$\alpha$ EWs require high inclinations, not unusually large covering factors.

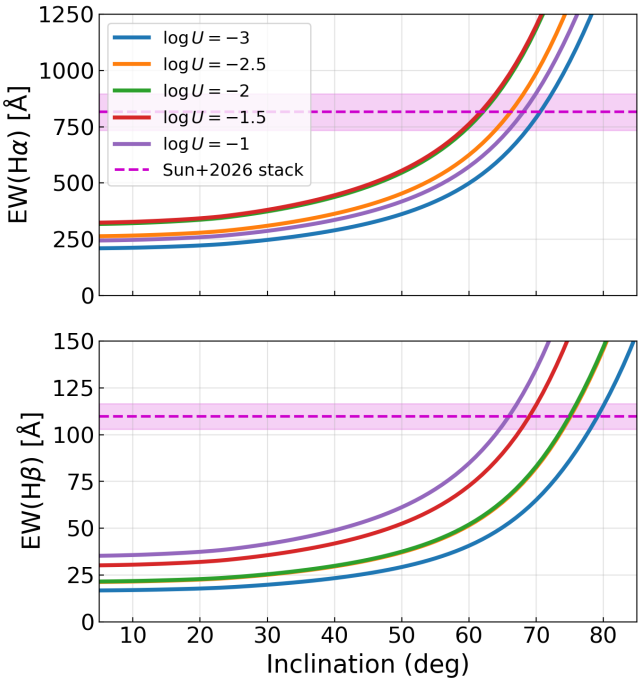


**Fig. 4.** Predicted inclination dependence of the Balmer EWs. The top and bottom panels show EW(H$\alpha$) and EW(H$\beta$), respectively, as functions of observer inclination for our fiducial super-Eddington model with $M_{\rm BH} = 10^{7.5}\,M_\odot$ and $\dot{m} = 32$. Curves correspond to different ionization parameters $\log U$ (legend), computed for a fixed BLR covering factor $C_{\rm BLR} = 0.15$. The magenta dashed lines and shaded bands indicate the total (broad+narrow) EWs measured from the median-stacked LRD spectrum of Sun et al. (2026), EW(H$\alpha$) $= 817.2^{+80.9}_{-82.7}$ and EW(H$\beta$) $= 109.8^{+6.8}_{-6.9}$; at the PRISM resolution these values cannot in general be decomposed into broad and narrow components. In our model, matching the large Balmer EWs favours highly inclined sightlines, typically $i \gtrsim 65°$–$70°$ depending weakly on $\log U$.

### 3.1. The missing hard photons problem of LRDs

One proposed explanation for the extreme X-ray weakness of JWST-discovered BLAGNs invokes heavy (Compton-thick) absorption by dense gas along the line of sight (e.g., Maiolino et al. 2025; Ji et al. 2025b). Columns as large as $N_{\rm H} \gtrsim 10^{25}\,{\rm cm}^{-2}$ must have a very low dust-to-gas ratio to allow for the detection of broad lines; BLR clouds could, in principle, satisfy this requirement. In LRDs, this interpretation has been linked to reports of deep Balmer absorption and non-stellar Balmer breaks, which imply high-density gas along the line of sight (Juodžbalis et al. 2024; D'Eugenio et al. 2026; Ji et al. 2025b; Naidu et al. 2025). However, the same explanation is difficult to extend to LBDs, which are also X-ray undetected even in stacking analyses, yet show no evidence for Balmer absorption or other signatures of dense intervening gas (Maiolino et al. 2025; Brazzini et al. 2026).

A related puzzle is that, while JWST spectra of LRDs and LBDs show strong broad Balmer emission, high-ionization lines such as HeII, CIV, and NV are often weak or undetected, pointing to an ionizing continuum incident on the line-emitting gas that differs from a standard quasar

power-law SED (Zucchi et al. 2025). One proposed explanation is the "gas-enshrouded black hole" scenario (e.g., Kido et al. 2025; Naidu et al. 2025), in which a compact, extremely dense HI envelope absorbs EUV and X-ray photons and reprocesses them into a softer continuum. This picture faces basic geometric and radiative-transfer difficulties: if the cocoon lies inside the BLR, it would severely limit the escape of ionizing photons, implying that the BLR must be ionized externally; if it lies outside the BLR, the broad lines should be strongly suppressed or hidden, since the putative atmosphere is assumed to be optically thick, thermalized, and to emit approximately as a blackbody with $T \sim 5000\,\mathrm{K}$.

Alternatively, in super–Eddington funnel geometries, the X-ray weakness is naturally explained by a Compton-cooled corona and, additionally, by orientation-dependent spectral shaping (Madau 2025). In these models the EUV band (600–900, ) remains blue and only moderately inclination-dependent, with $\beta_{\rm EUV} \simeq -2.1$ for face-on views and flattening to $\beta_{\rm EUV} \simeq -1.5$ near the equatorial plane, whereas the harder XUV band (200–600, ), which controls the production of high-ionization species, is strongly suppressed in equatorial directions and its slope changes from $\beta_{\rm XUV} \simeq -1.9$ face-on to $\beta_{\rm XUV} \simeq -0.14$ near the equatorial plane. Around the $He^+$ edge (54.4,eV), this strong XUV softening naturally reduces HeII (and related) emission while preserving strong Balmer lines.

Figure 5 compares our CLOUDY predictions for HeII $\lambda$4686/H$\beta$ to the observational upper limit for the LRD Abell 2744–QSO1. The model curves show the predicted ratio as a function of ionization parameter for super-Eddington SEDs with different black hole masses and accretion rates (see legend; the dot-dashed curve shows the single higher-density case). The hardest track ($M_{\rm BH} = 10^{7.7}\,M_\odot$, $\dot{m} = 12$) exceeds the upper limit across the full $\log U$ range, whereas the softer SEDs at higher $\dot{m}$ and/or larger $M_{\rm BH}$ satisfy the constraint. The black hole mass directly measured in Abell 2744–QSO1 by Juodžbalis et al. (2025b) is

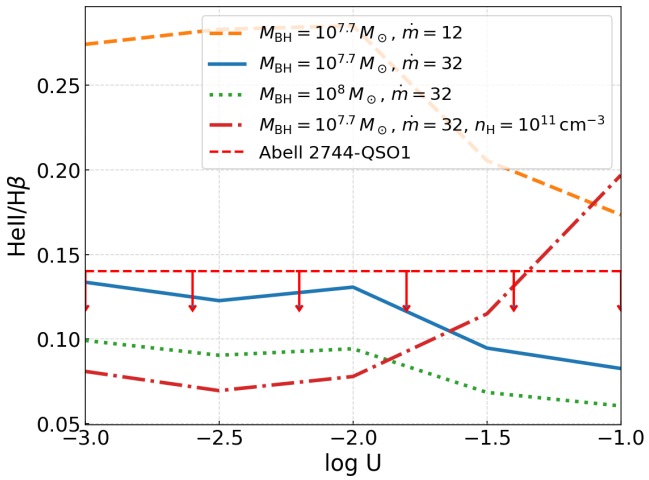


**Fig. 5.** Predicted HeII $\lambda$4686/H$\beta$ as a function of $\log U$ for super-Eddington SEDs of different $M_{\rm BH}$ and $\dot{m}$ (see legend). Unless otherwise noted, $n_{\rm H} = 10^{10}\,\mathrm{cm}^{-3}$; the single alternative-density case is labeled in the legend. The dashed line shows the upper limit for the LRD Abell 2744–QSO1 from JWST spectroscopy (Furtak et al. 2024; Ji et al. 2025b). All models assume $Z = 0.1\,Z_\odot$ and $N_{\rm H} = 10^{23}\,\mathrm{cm}^{-2}$.

$\log(M_{\rm BH}/M_\odot) \simeq 7.7$, consistent with single-epoch measurements (Furtak et al. 2024; Ji et al. 2025b; D'Eugenio et al. 2025a). The relatively low $\lambda_{\rm Edd}$ reported in previous work likely reflects standard bolometric corrections tied to broad H$\alpha$ and local quasar SED templates; dust attenuation and SED anisotropy can bias such inferences and allow for substantially higher intrinsic $\lambda_{\rm Edd}$ in our framework (see below).

### 3.2. Dust reddening and V-shaped SEDs

In our orientation-based picture linking LBDs and LRDs, the two populations correspond to the same underlying BLAGN class viewed at different inclinations: LBDs are preferentially seen intermediate-lower inclinations, while LRDs are those BLAGNs observed closer to the equatorial plane. Along these high-inclination sightlines, substantial dust attenuation is required to transform an intrinsically blue, super-Eddington AGN SED into the observed red rest-optical continuum. A number of recent analyses of LRDs have invoked extinctions of $A_V \sim$ a few magnitudes (e.g., Killi et al. 2024; Brooks et al. 2025; Li et al. 2025; Schindler et al. 2025; Akins et al. 2025a; Ji et al. 2025b; Brazzini et al. 2026). In this framework, the reddening is naturally attributed to an equatorial dusty torus located on the outskirts of the BLR or immediately beyond it, where the gas lies outside the dust sublimation radius and can sustain a significant dust column. Such a configuration provides a direct physical connection between the persistence of broad emission lines and the strong continuum reddening: for a foreground dust screen, both the BLR lines and the local continuum at a given wavelength are attenuated by the same factor (so the EW is preserved), while the overall SED becomes strongly reddened and bluer broad-line and continuum features are preferentially suppressed.

The dusty obscurer is modeled with the same clumpy formalism as the BLR (Eqs. 3–5), but with its own parameters ($C_{\rm dust}, \sigma_d$). Physically, a broader ("flared") angular distribution for the dusty component is expected because the dust-bearing obscurer resides at larger radii (beyond the dust sublimation front), where vertical support from radiation pressure on dust and/or disk winds can produce a larger scale height than in the dust-free BLR (e.g., Elitzur & Shlosman 2006; Nenkova et al. 2008; Elitzur 2008; Wada 2012). Concretely, we take

$$N_{{\rm los},d}(i) = N_{0,d}\,\exp\left[-\frac{\cos^2 i}{2\sigma_d^2}\right], \tag{7}$$

and

$$P_{{\rm esc},d}(i) = \exp\big[-N_{{\rm los},d}(i)\big], \tag{8}$$

and determine $N_{0,d}$ by requiring that the solid-angle averaged probability of encountering at least one dusty cloud equals the global dust covering factor,

$$C_{\rm dust} = \int_0^{\pi/2} \big[1 - P_{{\rm esc},d}(i)\big]\,\sin i\,{\rm d}i. \tag{9}$$

A value of $C_{\rm dust} = C_{\rm BLR} \simeq 0.15$ is consistent with the incidence of strongly reddened (LRD-like) objects within the parent BLAGN population (e.g., Hainline et al. 2025). We adopt a more flared dusty distribution than the BLR, with

$\sigma_d = 0.5$. This choice implies that dust-intersecting sightlines are typically viewed at high inclinations, with a conditional median $i_d \simeq 70°$. In this two-component scheme, $C_{\rm dust}$ sets the overall fraction of dust-intersecting sightlines, while the inclination distribution of dust-intersecting objects is given by the solid-angle weighted conditional probability

$$p(i \,|\, d) \propto \left[1 - P_{{\rm esc},d}(i)\right] \sin i, \tag{10}$$

i.e. random orientations ($\propto \sin i$) reweighted by the probability of intersecting at least one dusty cloud. Throughout this section, since our SED comparisons are conditioned on LRD selection, we apply dust attenuation deterministically along dust-intersecting sightlines.

The intrinsic SED (continuum plus emission lines) at inclination $i$ is mapped to the observed one via

$$\left[F_{\lambda,{\rm cont}}(\lambda;i) + F_{\lambda,{\rm line}}(\lambda)\right] \longrightarrow$$
$$\left[F_{\lambda,{\rm cont}}(\lambda;i) + F_{\lambda,{\rm line}}(\lambda)\right] 10^{-0.4\,A_\lambda(i)}, \tag{11}$$

with $A_\lambda(i) = A_V\,k(\lambda)$, where $k(\lambda)$ is the adopted extinction curve and $A_V$ is a free parameter setting the characteristic dust column along dust-intersecting sightlines – and $A_\lambda(i) = 0$ for clear sightlines.

We apply the Cardelli et al. (1989) extinction law, using the flexible Conroy et al. (2010) parameterization to vary the strength of the 2175 Å feature. We adopt a relatively high $R_V = 4$, yielding a flatter optical-UV curve consistent with dust in dense, processed environments, and set the UV-bump parameter to $B = 0.15$, i.e. a strongly suppressed 2175 Å Drude component compared to the standard Milky Way curve. This choice produces a relatively smooth, reddened UV continuum broadly consistent with that observed in LRDs (see also Killi et al. 2024; Li et al. 2025), and is physically motivated if the dust in these high-$z$ systems is metal-poor and/or has grain properties that differ from the local Milky Way ISM. Note that the adopted gray reddening curve remains steeper in the far-UV ($\lambda < 3000$ Å) than the notably flat AGN extinction law proposed by Gaskell et al. (2004).

Figure 6 compares the predicted SED of our fiducial super-Eddington models, attenuated by a dust screen with $A_V = 2.9$, to the composite UV-near-IR SED of a large, homogeneously selected sample of LRDs from multiple JWST Legacy fields with median redshift $\langle z \rangle \simeq 6.2$ (Delvecchio et al. 2025). The resulting V-shaped SED closely resembles the observed optical-UV spectrum of LRDs, with no evident need for a significant additional stellar contribution or AGN scattered light.[1] For a detailed quantitative comparison, we computed mock broadband filter fluxes by integrating the reddened model spectrum over the specific rest-frame bandpasses corresponding to the observations. Over 1250 Å–1.4 $\mu$m, the model reproduces the UV–optical SED with a mean model-to-data flux ratio of 1.05 and an rms scatter of 10%, which likely reflects a combination of intrinsic object-to-object variance in the parent LRD population and the finite-width bandpass averaging of strong spectral features. With an assumed high ionization parameter $\log U = -1.5$, high gas density ($n_{\rm H} = 10^{10}\,{\rm cm}^{-3}$), and column density ($N_{\rm H} = 10^{23}\,{\rm cm}^{-2}$), the processed continuum (transmitted plus nebular emission) can exhibit a sizeable Balmer discontinuity, with a clear contribution from Balmer-edge (continuum bound-free) absorption imprinted by the BLR gas on the transmitted component. In the composite observed SED, however, this feature is totally diluted by inclination-dependent mixing between the direct disk continuum and the processed component, yielding no break in the median stack. A more pronounced Balmer break is expected only in a sub-population of LRDs for which the direct continuum is largely suppressed (i.e. $P_{\rm esc}(i) \ll 1$) and the observed spectrum is dominated by transmitted-plus-nebular emission; such objects should preferentially correspond to the most strongly attenuated, near-equatorial sightlines in our orientation-based picture.

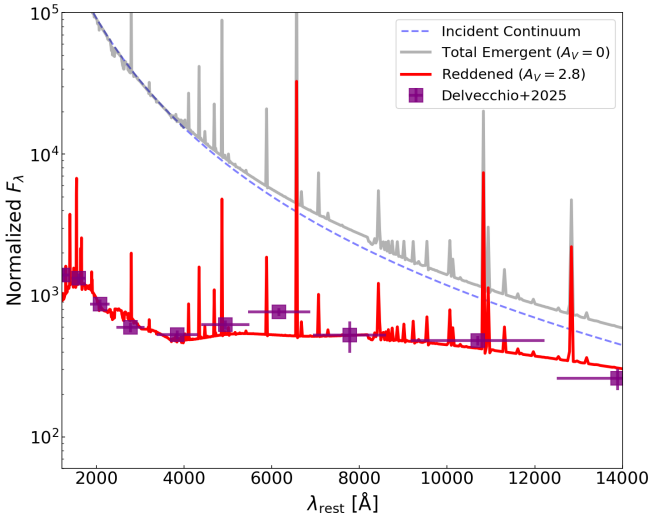


**Fig. 6.** Comparison of the stacked photometry of LRDs from Delvecchio et al. (2025) (purple squares) with a theoretical dust-attenuated accretion disk model. Fluxes are normalized at 7800 Å. The gray line shows the total emergent spectrum (continuum plus lines) from our super-Eddington accretor ($M_{\rm BH} = 10^{7.5}\,M_\odot$, $\dot{m} = 32$) after BLR processing (computed with Cloudy; no dust attenuation applied). The model curves are shown for an observer at inclination 70°, representative of dust-intersecting (LRD) sightlines for our adopted dusty angular distribution. The Cloudy parameters are $\log U = -1.5$, $n_{\rm H} = 10^{10}\,{\rm cm}^{-3}$, $N_{\rm H} = 10^{23}\,{\rm cm}^{-2}$. The red line shows the final spectrum after attenuation by a dust screen ($A_V = 2.8$) assuming a modified Cardelli et al. (1989) extinction law with $R_V = 4$ and $B = 0.15$ (see main text for details). With a covering factor of $C_{\rm BLR} = 0.15$, this fiducial model appears to reproduce the V-shaped SED observed in LRDs.

A direct observational corollary of the dusty, inclination-dependent component in our model is a large Balmer decrement: extinction suppresses H$\beta$ more strongly than H$\alpha$, so even a moderately elevated intrinsic broad-line ratio $({\rm H}\alpha/{\rm H}\beta)_{\rm int}$ is readily driven to the high values inferred for LRDs along dust-obscured sightlines. For our fiducial BLR spectrum we obtain $({\rm H}\alpha/{\rm H}\beta)_{\rm int} \simeq 4.6$; applying the same line-of-sight attenuation, $A_V = 2.8$, required by the LRD SED fits naturally yields $({\rm H}\alpha/{\rm H}\beta)_{\rm obs} \simeq 10.0$. Fig-

[1] We suppress the intrinsic Ly$\alpha$ and He I $\lambda$10830 emission components in our model. This is motivated by the very large line optical depths expected in heavily obscured environments: Ly$\alpha$ photons undergo resonant trapping, while He I $\lambda$10830 can become optically thick due to the metastable $2^3S$ lower level. In both cases, repeated scatterings increase the effective path length and enhance the probability of absorption by dust, plausibly reducing the emergent line flux in LRDs.

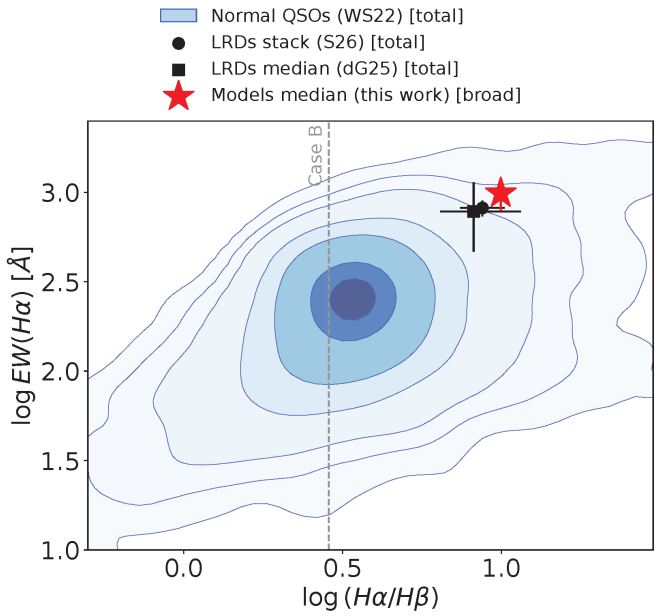


**Fig. 7.** Rest-frame H$\alpha$ EW versus Balmer decrement. The red star marks the value from our super-Eddington model matched to the stacked LRD spectrum (broad H$\alpha$ component). Filled symbols show literature measurements for JWST LRDs: the median of the de Graaff et al. (2025) LRD sample and the stacked LRD spectrum of Sun et al. (2026). For the de Graaff et al. point, the horizontal and vertical error bars denote the 16th and 84th percentiles of the observed distributions in H$\alpha$/H$\beta$ and EW(H$\alpha$), respectively. Gray contours show the locus of $z \simeq 0$–0.6 SDSS broad-line quasars from the DR16Q compilation of Wu & Shen (2022). The dotted line indicates the Case B recombination value (H$\alpha$/H$\beta$) = 2.86. Our model lies on an extreme but continuous extension of the trend defined by classical AGNs toward larger EW(H$\alpha$) and Balmer decrements.

ure 7 places this result in the plane of EW(H$\alpha$) versus H$\alpha$/H$\beta$: the model point (red star) lies at the high-EW, high-decrement end of the $z \simeq 0$–0.6 SDSS quasar locus (Wu & Shen 2022), and is consistent with current JWST LRD constraints from both the median of the de Graaff et al. (2025) sample and the stacked LRD spectrum of Sun et al. (2026). In this sense, our model appears as a continuous, albeit extreme, extension of classical type-1 AGN properties rather than a qualitatively distinct population (c.f. Sun et al. 2026). We emphasize that Case B is not expected to hold exactly in BLR conditions, where collisional processes and line optical depths can elevate the intrinsic decrement (indeed, our fiducial H$\alpha$/H$\beta \simeq 4.6$ already reflects such departures), but recent multi-line JWST analyses find that the broad-line ratios in most LRDs remain consistent with dust-reddened recombination, with only rare outliers requiring additional radiative-transfer effects (Nikopoulos et al. 2025; D'Eugenio et al. 2025b).

In our orientation-based picture, LRDs represent the high-decrement tail of the BLAGN population: along obscured, near-equatorial sightlines the same dusty, low-ionization gas that reddens the continuum preferentially attenuates H$\beta$ relative to H$\alpha$. By contrast, the bluer, less-obscured LBDs are viewed along relatively clear sightlines, so their Balmer decrements should remain close to the intrinsic BLR ratio (i.e. only mildly above Case B), with intermediate objects naturally populating the transition regime.

### 3.3. No dust budget crisis in LRDs

A commonly noted tension for dust-reddened interpretations of LRDs is an "IR-energy (dust budget) crisis": extinctions of $A_V \gtrsim$ a few magnitudes, when coupled with an effectively enclosing dusty screen (solid angle $\Omega \sim 4\pi$), would intercept a large fraction of the bolometric output and predict strong mid-IR to (sub)mm re-radiation, in tension with the faint stacked or non-detected infrared emission in several samples, including the most luminous systems (e.g., Chen et al. 2025; Setton et al. 2025).

At the same time, stacking analyses have recently revealed an AGN-heated hot-dust component in the median LRD SED, rising into the rest-frame near-IR, and argued that the dust geometry must leave at least part of the optical/UV continuum and BLR emission unobscured (Delvecchio et al. 2025). Recent Rosetta Stone case studies likewise find clear evidence for AGN-heated hot dust in both the LRD archetype GN–28074 and the LBD archetype GS–3073 (Brazzini et al. 2026). In addition, SED modeling of local LRD analogs indicates that hot (torus) dust can dominate the rest-frame near-IR: Ji et al. (2025a), for example, find that the best-fit emission around $\sim 5\,\mu$m is dominated by hot dust from the torus, while Lin et al. (2026) report significant hot-dust emission in local LRDs. In our inclination-based framework this is consistent with a modest global dust covering factor: while dust reradiation is approximately isotropic, only a small fraction $C_{\rm dust}$ of the bolometric luminosity is intercepted and reprocessed, allowing a hot-dust rise in the near–IR without the large IR power expected for fully enshrouding (near-unity covering) models.

We model the infrared reprocessing by dust using an energy-balance calculation. Given an intrinsic (unreddened) incident spectrum $L_{\nu,\rm inc}$, dust at radius $r$ absorbs a fraction of the radiation field and re-emits thermally. In practice, rather than solving explicitly for $T_{\rm d}(r)$ from a frequency-dependent radiative-equilibrium equation, we adopt a parametric temperature profile anchored at the sublimation radius and normalize the dust emission by enforcing bolometric energy conservation. Specifically, we take

$$T_{\rm d}(r) = T_{\rm sub}\left(\frac{r}{r_{\rm in}}\right)^{-1/2}, \qquad r_{\rm in} \le r \le r_{\rm out}, \tag{12}$$

as expected for radiative equilibrium with approximately gray dust heated by a central source. Here, $r_{\rm in}$ is set by dust sublimation, $T_{\rm d}(r_{\rm in}) = T_{\rm sub}$. The absorbed luminosity is computed directly from the difference between the unreddened and reddened continua implied by the adopted extinction curve,

$$L_{\rm abs} = \int_0^\infty \left[L_{\nu,\rm inc} - L_{\nu,\rm inc}\, 10^{-0.4A_\lambda}\right] {\rm d}\nu, \tag{13}$$

so that the wavelength dependence of dust opacity enters through $A_\lambda$ without requiring explicit specification of the extinction or absorption cross sections. Here $L_{\rm abs}$ should be interpreted as the bolometric power removed from the incident spectrum along a representative dust-obscured line of sight; the total power reprocessed by dust is then reduced by the global covering factor $C_{\rm dust}$.

We assume a power-law radial density profile for the dusty gas,

$$n(r) = n_0\left(\frac{r}{r_{\rm in}}\right)^{-q}, \qquad r_{\rm in} \le r \le r_{\rm out}, \tag{14}$$

and construct the (unnormalized) re-emitted spectrum as a superposition of modified blackbodies,

$$L_{\nu,\rm dust} \propto \kappa_\nu \int_{r_{\rm in}}^{r_{\rm out}} B_\nu\left[T_{\rm d}(r)\right]\, n(r)\, 4\pi r^2\, {\rm d}r, \tag{15}$$

where we adopt an effective opacity law $\kappa_\nu \propto \nu^p$ with $p \simeq 0$. While our inferred attenuation curve is relatively flat ($R_V = 4$) and lacks a pronounced 2175 Å bump – suggesting a deficit of small carbonaceous particles and a bias toward larger grains in the UV/optical absorbing dust (e.g., Gaskell et al. 2004; Maiolino et al. 2001b,a) – this graybody approximation for the infrared emission is physically motivated by optical depth rather than intrinsic grain size. Given the extreme compactness and high column densities expected in the nuclei of these sources, the dust is likely distributed in dense, optically thick clumps (e.g., Nenkova et al. 2008). In this regime, the dust distribution can become optically thick even at far-infrared wavelengths. Because the emission is dominated by the optically thick surfaces of these clouds, radiative transfer effects and the superposition of clumps at various temperatures dilute intrinsic compositional spectral signatures. This effectively flattens the observed emissivity index to $p \simeq 0$, regardless of the intrinsic optical properties of the individual dust grains ($p \approx 2$ in the diffuse ISM), making the emergent infrared continuum well-approximated by a graybody.

Finally, we set the normalization by requiring that the integrated dust emission equals a fraction $C_{\rm dust}$ of the absorbed luminosity,

$$\int_0^\infty L_{\nu,\rm dust}\, {\rm d}\nu \;=\; C_{\rm dust}\, L_{\rm abs}. \tag{16}$$

In the fiducial configuration used in Figure 8 we adopt $q = 0.5$, a sublimation temperature $T_{\rm sub} = 1200\,{\rm K}$, and a radial extent $r_{\rm out}/r_{\rm in} = 100$. These choices produce a broad mid-IR bump peaking at $\lambda_{\rm rest} \sim 20\,\mu$m that matches the Delvecchio et al. composite while keeping the far-infrared tail consistent with current limits, and they lie within the range of slopes and radial extents commonly inferred for AGN dusty tori in clumpy and smooth models (e.g., Fritz et al. 2006; Nenkova et al. 2008; Stalevski et al. 2012).

Although our phenomenological dust model is not explicitly parameterized in terms of a total dust mass, the implied $M_{\rm dust}$ is very small. For the extinctions relevant to LRDs ($A_V \simeq 3$ along obscured sightlines), and assuming $D/G \propto Z$ with $Z \sim 0.1\,Z_\odot$, the reduced dust-to-gas ratio ($\sim 1/1000$) implies a higher gas column, $N_{\rm H} \sim (5\times10^{22}$–$10^{23})\,{\rm cm}^{-2}$. For our compact structure with $C_{\rm dust} = C_{\rm BLR} = 0.15$, $r_{\rm in} \sim 0.15\,{\rm pc}$, $r_{\rm out}/r_{\rm in} = 100$, and $n \propto r^{-q}$ with $q = 0.5$, this corresponds to a total gas mass $M_{\rm gas} \sim$ few $\times\, 10^4$–$10^5\,M_\odot$ and hence $M_{\rm dust} \sim 30$–$100\,M_\odot$. This is far below ALMA stacking upper limits for typical LRDs ($M_{\rm dust} \lesssim 10^6\,M_\odot$ at $z \sim 6$; Casey et al. 2025; Chen et al. 2025; Setton et al. 2025) and is therefore consistent with the dust-budget constraints ("dust budget crisis") at high redshift (Chen et al. 2025).

## 4. Discussion and summary

The physical nature of LRDs remains debated. Purely stellar interpretations invoke compact, evolved stellar populations with strong nebular emission to explain the V–shaped SEDs (e.g., Baggen et al. 2024; Pérez-González et al. 2024; Leung et al. 2025; Labbe et al. 2025; Hainline et al. 2025), but several lines of evidence increasingly favour an AGN–dominated optical continuum in at least a substantial fraction of LRDs: the prevalence of broad Balmer lines and extreme Balmer EWs (Hviding et al. 2025; Yan et al. 2025), the frequent dominance of an unresolved rest–optical component (Hviding et al. 2025; Killi et al. 2024), and spectroscopic signatures around the Balmer break that are more naturally explained by absorption and radiative transfer in high-density gas than by an old stellar continuum (Juodžbalis et al. 2024; Ji et al. 2025b; Inayoshi & Maiolino 2025; D'Eugenio et al. 2025a; Yan et al. 2025).

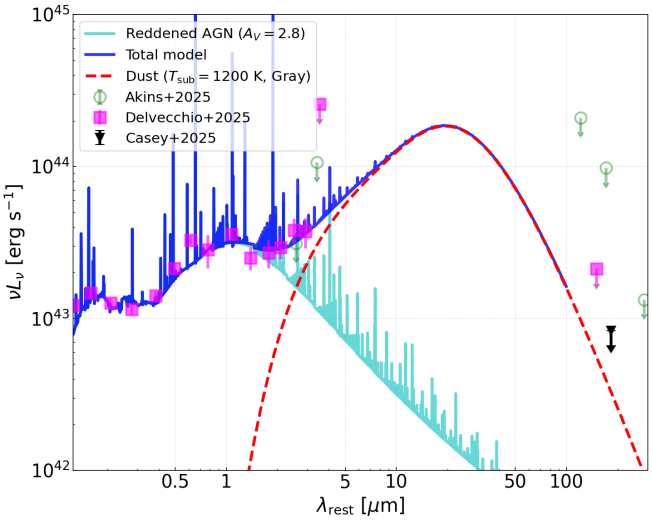


**Fig. 8.** Rest-frame $\nu L_\nu$ SED illustrating the dust-reprocessed emission in our LRD model. The cyan curve shows the reddened super-Eddington AGN continuum for $A_V = 2.5$, normalized to the Delvecchio et al. composite at $\lambda_{\rm rest} \simeq 7800$ Å. The red dashed curve is the dust re-emission computed from the absorbed luminosity using a multi-temperature blackbody with $T_{\rm sub} = 1200\,{\rm K}$, a radial density profile $n \propto r^{-0.5}$, and $r_{\rm out}/r_{\rm in} = 100$, scaled by a dust covering factor $C_{\rm dust} = 0.15$. The solid blue curve is the total model (reddened AGN plus dust). Magenta squares show the stacked LRD photometry from Delvecchio et al. (2025), while green open circles and the black arrow indicate the infrared and sub-mm upper limits from the Akins et al. (2025a) stack and from Casey et al. (2025), respectively. The model reproduces the observed near-IR rise of LRDs while remaining consistent with current constraints at $\lambda_{\rm rest} \gtrsim 50\,\mu$m, thereby avoiding a dust-mass or IR-energy budget crisis.

Motivated by this empirical picture and by the emerging LBD/LRD taxonomy, we have explored a unified AGN framework in which LRDs and LBDs share a common, super-Eddington central engine and differ primarily by orientation and line–of–sight obscuration. At $z \gtrsim 6$ the nuclei of galaxies are typically extremely gas rich and rapidly fed by cold inflows and violent disk instabilities, while the black holes are still comparatively small; at fixed physical supply rate $\dot{M}$, the dimensionless accretion rate $\dot{m}$ is therefore naturally large, so early growth is expected to proceed through frequent or sustained super-Eddington episodes in many models (e.g., Madau et al. 2014; Lupi et al. 2016; Huško et al. 2025).

H$\alpha$ EW. A first key result concerns the extreme broad H$\alpha$ EWs of LRDs. Using super-Eddington thick–disk SEDs, we have constructed BLR photoionization models that include anisotropic illumination and an inclination–dependent continuum decomposition. When the inclination distribution is folded in, matching the probability–weighted median H$\alpha$ EW of the JWST BLAGN sample ($\simeq$ 570 Å; Maiolino et al. 2025) requires global BLR covering factors of only $C_{\rm BLR} \simeq 0.15$ (see also Madau 2025). These values are fully consistent with standard estimates for low–$z$ Type 1 AGNs (e.g., Peterson 2006; Pandey et al. 2023) and stand in contrast to models that invoke nearly $4\pi$ coverage by dense gas in order to reproduce the same EWs with canonical quasar SEDs (Yan et al. 2025). In our framework, the large EWs arise from two coupled effects: a harder, ionizing-rich intrinsic SED that enhances the line production efficiency, and an anisotropic radiation field in which high–inclination sightlines suffer strong continuum dilution as the hot inner funnel becomes self–shadowed. The most extreme LRDs therefore correspond to high–inclination views of modest–covering BLRs, rather than to enshrouded, unity–covering geometries. We predict that less–reddened LBDs should preferentially exhibit lower EWs, whereas obscured, high–inclination LRDs should populate the high–EW tail.

High-ionization lines. Second, the model accounts for the lack of strong high–ionization UV lines in many LRDs and related JWST BLAGNs (Madau 2025). Because the XUV band that controls $He^+$ and higher ions is strongly suppressed toward equatorial sightlines, the predicted HeII $\lambda$4686/H$\beta$ ratios fall well below the upper limits in systems such as Abell 2744–QSO1 for plausible combinations of $M_{\rm BH}$, $\dot{m}$, and ionization parameter. In this view, the "missing hard photons" problem of LRDs is an outcome of orientation–dependent spectral shaping in super-Eddington funnels, rather than evidence for an extremely dense, fully enclosing neutral envelope. In the same scenario X-ray emission is intrinsically suppressed by Compton-cooling of the corona.

V-shaped SED. Third, an intrinsically blue super-Eddington SED combined with modest equatorial dust reddening reproduces the characteristic V–shaped UV–optical SEDs of LRDs. Adopting a modified Cardelli et al. (1989) extinction law with $R_V = 4$ and a strongly suppressed 2175 Å bump ($B = 0.15$) yields an effective curve similar to the flatter, weak–bump extinction laws inferred for high–$z$ galaxies, while remaining steeper in the far–UV than the very gray AGN curve of Gaskell et al. (2004). For $A_V \simeq 2.8$ along obscured sightlines, our fiducial model reproduces well the stacked LRD SED of Delvecchio et al. (2025) from rest–frame 1250 Å to 1.4 $\mu$m.

It has been recently suggested that the rest-UV component of LRD spectra is primarily associated with the host galaxy, motivated in part by the anti-correlation between EW([OIII] $\lambda$5007) and the Balmer break, as well as by the correlation between the [OIII] and UV luminosities (de Graaff et al. 2025). We caution against overinterpreting these relations. First, both EW([OIII]) and the Balmer break depend on the optical continuum level, so some degree of correlation is expected even in the absence of a causal link. Second, luminosities of different tracers tend to correlate because they share the common luminosity-distance factor.

Independently of the above, weak [O III] emission in the LRDs with the strongest Balmer breaks may not require the UV continuum to be host-dominated. In luminous quasars, the EW([OIII]) is known to decrease with increasing luminosity (a "narrow-line Baldwin effect") and has also been interpreted as a consequence of the narrow-line region (NLR) becoming so extended that it effectively runs out of ambient gas to ionize. Either effect could be accentuated in very compact systems. Moreover, if LRDs are preferentially selected along dust-attenuated sightlines with $A_V \sim 2.8$, they may be biased toward intrinsically higher luminosities (by up to order-of-magnitude factors) in flux-limited samples. In this case, their unobscured counterparts would correspond to the most luminous LBDs, potentially overlapping with the quasar regime, and a reduced EW([OIII]) could arise from such selection bias without invoking a dominant stellar UV component. A detailed analysis of the specific physical conditions within the NLR of these BLAGNs is beyond the scope of this paper and will be addressed in future work.

The finding of spatially offset blue components is more compelling evidence for host-galaxy contributions (e.g., Baggen et al. 2026); however, while a substantial fraction of LRDs show offset blue light, only a subset are sufficiently close to contaminate the spectrum extracted at the LRD position, whereas many of the remaining offsets may be more relevant for Lyman–Werner irradiation than for the observed UV continuum. Moreover, in a number of systems the UV and optical components are coincident, including strongly lensed cases (e.g., Furtak et al. 2024), and in others the spectral diagnostics unambiguously associate the UV component with the AGN (e.g., Labbe et al. 2024). It is plausible that in some LRDs the UV may be host-dominated. In that case, our scenario would still apply to the optical continuum and line emission, particularly if extinction is sufficiently high (or the attenuation curve sufficiently steep) to suppress the AGN contribution in the UV, as may be the case for the LRDs with very weak UV emission (e.g., Naidu et al. 2025).

Balmer absorption. In our picture, the Balmer discontinuity in the processed spectrum (transmitted plus nebular) is strongly diluted in the median stack by mixing with the direct disk continuum. Pronounced Balmer breaks are therefore expected only when the direct continuum is heavily suppressed and the observed SED is dominated by the processed component; by contrast, a V-shaped UV-optical continuum can arise from wavelength-dependent attenuation and component mixing even if the Balmer edge is modest. This is qualitatively consistent with the relatively small fraction of LRDs that exhibit strong Balmer breaks.

In our interpretation, the observability of Balmer absorption is regulated by two separable "gates". The first is a dust/obscuration gate: in classical low-$z$ unification, equatorial sightlines are typically extinguished enough that the BLR is hidden (Type 2), so any Balmer absorption would be unobservable. Such Type 2 extinctions are far larger than the moderate $A_V \simeq 3$ values relevant for LRD-like, partially obscured Type 1 sightlines. The second is a gas-physics gate: Balmer absorption requires a substantial

column of dense, partially neutral gas with an enhanced $n = 2$ population in front of the continuum source and sufficient covering to imprint troughs. In our framework, the required gas is naturally available along near-equatorial rays, primarily in BLR-associated material (and plausibly also in the molecular/atomic layers of the torus). At low $z$, however, these directions are usually rendered inaccessible by the large dust columns that produce Type 2 spectra. At high redshift, a reduced dust-to-gas ratio in chemically young nuclei can allow some near-equatorial sightlines to remain only moderately extincted, yielding LRD-like spectra in which broad Balmer emission and, in favourable cases, Balmer absorption remain observable. This is also consistent with the observed empirical coupling between UV slope and Balmer-break strength, with redder UV continua generally exhibiting stronger Balmer breaks (de Graaff et al. 2025). By contrast, LBDs correspond to lower-inclination views with little extinction and are therefore less likely to intersect the dense, partially neutral columns required for Balmer absorption.

Balmer decrement. The same dusty component that reddens the continuum also predicts large Balmer decrements along obscured sightlines. For our fiducial BLR model the intrinsic broad–line ratio is $(\mathrm{H}\alpha/\mathrm{H}\beta)_{\rm int} \simeq 4.6$, which is driven to $(\mathrm{H}\alpha/\mathrm{H}\beta)_{\rm obs} \simeq 10$ once the line-of-sight attenuation required by the SED fits is applied. These values are comparable to the high decrements measured in many LRDs and their correlation with UV slope (de Graaff et al. 2025). In our orientation-based unification, LRDs correspond to the high-decrement tail of the BLAGN population, where dusty, low–ionization gas along high-inclination sightlines both reddens the continuum and selectively suppresses H$\beta$; LBDs, viewed along relatively clear sightlines, retain Balmer decrements close to the intrinsic BLR value (which can be Case B or possibly deviating from it because of intrinsic radiative/collisional processes), with intermediate objects populating the transition regime.

Dusty torus. Finally, we have addressed the "IR–energy" or dust–budget crisis that afflicts heavily obscured interpretations of LRDs. Extinctions of $A_V \sim 3$ combined with a near–unity dust covering factor would reprocess a large fraction of the bolometric output into the infrared, apparently in tension with the faint or undetected mid–IR and (sub)mm emission seen in stacks and individual systems (e.g., Chen et al. 2025; Setton et al. 2025; Casey et al. 2025). Our energy–conserving dust model instead assumes a compact equatorially concentrated structure with a global covering factor of 15%, a standard power–law radial density profile, a sublimation temperature characteristic of AGN-heated dust, and a finite radial extent of order two decades in radius, normalized such that only a modest fraction of the dust-reprocessed luminosity emerges in the near-IR. This configuration produces a broad mid–IR bump peaking at $\lambda_{\rm rest} \sim 20\,\mu$m that matches the Delvecchio et al. stack and remains consistent with the Akins et al. and Casey et al. upper limits at $\lambda_{\rm rest} \gtrsim 50\,\mu$m. For the modest columns required to achieve $A_V \simeq 3$ along obscured sightlines and a reduced dust-to-gas ratio appropriate for metal-poor hosts, the implied dust mass in our torus is less than a hundred solar masses, orders of magnitude below current ALMA limits on the global dust content of LRD hosts. In this sense, the small covering, low–mass dusty structure invoked here is a natural way to reconcile the large line–of–sight reddenings with stringent constraints on integrated dust mass and IR luminosity.

Taken together, these results support an interpretation in which LRDs are not a distinct class of engines, but rather the obscured, high-inclination tail of a population of compact, super-Eddington BLAGNs, whose less-reddened, more face-on analogues are observed as LBDs. The combination of anisotropic, intrinsically blue SEDs, modest BLR and dust covering factors, and orientation-dependent continuum dilution appears capable of explaining, within a single framework, the defining phenomenology of LRDs: their extreme H$\alpha$ EWs, large Balmer decrements, weak high-ionization UV lines, V-shaped continua, muted IR output, and the generally low level of rest–UV/optical variability expected when the observed continuum is dominated by the geometrically thick outer flow and reprocessed emission.

Exponential Balmer wings have been reported in many LRDs, particularly in the highest–S/N JWST spectra where a double–sided exponential component is often statistically preferred, consistent with some contribution from electron scattering. However, recent Rosetta Stone analyses show that similar non–Gaussian, approximately exponential Balmer wings are not unique to LRDs but are also present in the LBD archetype, and even in standard low–$z$ Type 1 AGNs (Brazzini et al. 2026; Wada et al. 2026; Laor 2006). This implies that exponential wings alone do not require – nor uniquely diagnose – an LRD–specific, pc–scale nuclear cocoon (e.g., Torralba et al. 2025; Brazzini et al. 2026). In our scenario, approximately exponential Balmer wings can arise naturally from thermal Thomson scattering by free electrons within (or immediately surrounding) the BLR, for modest scattering optical depths compatible with BLR–scale columns and ionized fractions (as originally suggested by Laor 2006).

We note that a nearly $4\pi$ gas–enshrouded scenario has been invoked to explain the weak Ly$\alpha$ emission in one LRD at $z = 4.4$ (Torralba et al. 2026), on the grounds that the AGN ionizing continuum cannot escape in this system. However, this inference is based on a single object, and Ly$\alpha$ can be readily attenuated or destroyed by resonant scattering and absorption in neutral gas and dust in the CGM. Moreover, several other LRDs show clear evidence for prominent Ly$\alpha$ emission (e.g., Tripodi et al. 2025a; Morishita et al. 2025; Tripodi et al. 2025b; Ji et al. 2025b, Geris in prep.).

It has recently been reported that the detection of water absorption in two LRDs supports a scenario in which the observed optical/near–IR emission arises from a cool atmosphere surrounding the black hole (Wang et al. 2026). We argue instead that water absorption is naturally explained by a warm circumnuclear dusty torus, which is expected to lie along the line of sight for LRDs and can provide physical conditions conducive to molecular survival and formation. Indeed, water absorption is relatively common in AGNs, including in the local Universe, particularly among dust–obscured systems (e.g., García-Bernete et al. 2026; González-Alfonso et al. 2010). An additional contribution could arise from the host-galaxy stellar population in those two LRDs, which may become more prominent at longer wavelengths. Assessing this possibility would require a dedicated analysis beyond the scope of this paper.

Future tests of our LBD/LRD unification scheme should move beyond single-object comparisons and instead map the joint demographics of high-redshift BLAGNs to test a quantitatively predicted, orientation-based connection between LBDs and LRDs. This requires measuring the LRD/LBD number ratio versus luminosity, quantifying the incidence of Balmer breaks and the full Balmer-decrement distribution, and establishing how both correlate with UV-optical continuum shape and line EWs. A key requirement is to obtain robust, inclination-aware estimates of $M_{\rm BH}$ and $\lambda_{\rm Edd}$. In particular, current published values of $\lambda_{\rm Edd}$ for LRDs are typically $\lambda_{\rm Edd} \sim 0.2$–$0.5$, which may reflect systematics in standard luminosity inference rather than genuinely sub-Eddington accretion. Many studies estimate $L_{\rm bol}$ from broad H$\alpha$ luminosities using locally calibrated scaling relations that implicitly assume minimal internal attenuation and a near-universal quasar SED. If, as in our framework, the same dusty component that reddens the continuum also attenuates the broad Balmer lines, then $L_{\rm H\alpha}$ (and hence $L_{\rm bol}$) can be underestimated by large factors; moreover, if the intrinsic ionizing SED and its anisotropy differ from the local templates underlying these calibrations, the mapping between $L_{\rm H\alpha}$ and $L_{\rm bol}$ becomes orientation dependent. Taken together, dust attenuation and SED- and inclination-driven departures from local $L_{\rm H\alpha}$–$L_{\rm bol}$ conversions may help reconciling existing line-based $M_{\rm BH}$ estimates with substantially higher intrinsic $\lambda_{\rm Edd}$, as required by our model. Standard single-epoch virial methods may also be biased for a flattened BLR, so independent constraints from multi-line and multi-epoch spectroscopy, physically motivated BLR/disk-wind modeling, and bolometric consistency checks will be essential to confirm accretion rates $\dot{m} \gg 1$.

## References


Akins, H. B., Casey, C. M., Berg, D. A., et al. 2025a, ApJ, 980, L29

Akins, H. B., Casey, C. M., Lambrides, E., et al. 2025b, ApJ, 991, 37

Ananna, T. T., Bogdán, Á., Kovács, O. E., Natarajan, P., & Hickox, R. C. 2024, ApJ, 969, L18

Baggen, J. F. W., Scoggins, M. T., van Dokkum, P., et al. 2026, arXiv e-prints, arXiv:2602.02702

Baggen, J. F. W., van Dokkum, P., Brammer, G., et al. 2024, ApJ, 977, L13

Barro, G., Perez-Gonzalez, P. G., Kocevski, D., et al. 2025, arXiv e-prints, arXiv:2512.15853

Brazzini, M., D'Eugenio, F., Maiolino, R., et al. 2026, arXiv e-prints, arXiv:2601.22214

Brooks, M., Simons, R. C., Trump, J. R., et al. 2025, ApJ, 986, 177

Cardelli, J. A., Clayton, G. C., & Mathis, J. S. 1989, ApJ, 345, 245

Casey, C. M., Akins, H. B., Finkelstein, S. L., et al. 2025, ApJ, 990, L61

Chatzikos, M., Bianchi, S., Camilloni, F., et al. 2023, Rev. Mexicana Astron. Astrofis., 59, 327

Chen, K., Li, Z., Inayoshi, K., & Ho, L. C. 2025, ApJ, 994, L42

Conroy, C., Schiminovich, D., & Blanton, M. R. 2010, ApJ, 718, 184

de Graaff, A., Hviding, R. E., Naidu, R. P., et al. 2025, arXiv e-prints, arXiv:2511.21820

de Graaff, A., Rix, H.-W., Naidu, R. P., et al. 2025, Astronomy & Astrophysics, 677, A56

Delvecchio, I., Daddi, E., Magnelli, B., et al. 2025, arXiv e-prints [arXiv:2509.07100]

D'Eugenio, F., Juodžbalis, I., Ji, X., et al. 2026, MNRAS, 545, staf2117

D'Eugenio, F., Maiolino, R., Perna, M., et al. 2025a, arXiv e-prints, arXiv:2503.11752

D'Eugenio, F., Nelson, E., Ji, X., et al. 2025b, arXiv e-prints, arXiv:2510.00101

Du, R., Ho, L. C., Ding, Y., & Li, R. 2025, ApJ, 988, 3

Elitzur, M. 2008, New A Rev., 52, 274

Elitzur, M. & Shlosman, I. 2006, ApJ, 648, L101

Fritz, J., Franceschini, A., & Hatziminaoglou, E. 2006, MNRAS, 366, 767

Furtak, L. J., Labbé, I., Zitrin, A., et al. 2024, Nature, 628, 57

García-Bernete, I., Pereira-Santaella, M., González-Alfonso, E., et al. 2026, arXiv e-prints, arXiv:2602.04967

Gaskell, C. M. 2009, New A Rev., 53, 140

Gaskell, C. M., Goosmann, R. W., Antonucci, R. R. J., & Whysong, D. H. 2004, ApJ, 616, 147

González-Alfonso, E., Fischer, J., Isaak, K., et al. 2010, A&A, 518, L43

Greene, J. E., Labbe, I., Goulding, A. D., et al. 2024, ApJ, 964, 39

Hainline, K. N., Maiolino, R., Juodžbalis, I., et al. 2025, ApJ, 979, 138

Harikane, Y., Zhang, Y., Nakajima, K., et al. 2023, ApJ, 959, 39

Hutsemékers, D., Sluse, D., Savić, D. V., & Richards, G. T. 2023, A&A, 672, A45

Huško, F., Lacey, C. G., Roper, W. J., et al. 2025, MNRAS, 537, 2559

Hviding, R. E., de Graaff, A., Miller, T. B., et al. 2025, A&A, 702, A57

Inayoshi, K. & Maiolino, R. 2025, ApJ, 980, L27

Ji, X., D'Eugenio, F., Juodžbalis, I., et al. 2025a, MNRAS[arXiv:2507.23774]

Ji, X., Maiolino, R., Übler, H., et al. 2025b, MNRAS, 544, 3900

Jiang, Y.-F., Stone, J. M., & Davis, S. W. 2014, ApJ, 796, 106

Juodžbalis, I., Ji, X., Maiolino, R., et al. 2024, MNRAS, 535, 853

Juodžbalis, I., Maiolino, R., Baker, W. M., et al. 2025a, arXiv e-prints, arXiv:2504.03551

Juodžbalis, I., Marconcini, C., D'Eugenio, F., et al. 2025b, arXiv e-prints, arXiv:2508.21748

Kido, D., Ioka, K., Hotokezaka, K., Inayoshi, K., & Irwin, C. M. 2025, MNRAS, 544, 3407

Killi, M., Watson, D., Brammer, G., et al. 2024, A&A, 691, A52

Kocevski, D. D., Finkelstein, S. L., Barro, G., et al. 2025, ApJ, 986, 126

Labbe, I., Greene, J. E., Bezanson, R., et al. 2025, ApJ, 978, 92

Labbe, I., Greene, J. E., Matthee, J., et al. 2024, arXiv e-prints, arXiv:2412.04557

Lambrides, E., Garofali, K., Larson, R., et al. 2024, arXiv e-prints, arXiv:2409.13047

Laor, A. 2006, ApJ, 643, 112

Leung, G. C. K., Finkelstein, S. L., Pérez-González, P. G., et al. 2025, ApJ, 992, 26

Li, Z., Inayoshi, K., Chen, K., Ichikawa, K., & Ho, L. C. 2025, ApJ, 980, 36
Lin, X., Fan, X., Cai, Z., et al. 2026, ApJ, 997, 364
Lupi, A., Haardt, F., Dotti, M., et al. 2016, MNRAS, 456, 2993
Lupi, A., Trinca, A., Volonteri, M., Dotti, M., & Mazzucchelli, C. 2024, A&A, 689, A128
Madau, P. 1988, ApJ, 327, 116
Madau, P. 2025, arXiv e-prints, arXiv:2501.09854
Madau, P. & Haardt, F. 2024, ApJ, 976, L24
Madau, P., Haardt, F., & Dotti, M. 2014, ApJ, 784, L38
Maiolino, R., Marconi, A., & Oliva, E. 2001a, A&A, 365, 37
Maiolino, R., Marconi, A., Salvati, M., et al. 2001b, A&A, 365, 28
Maiolino, R., Risaliti, G., Signorini, M., et al. 2025, MNRAS, 538, 1921
Maiolino, R., Scholtz, J., Curtis-Lake, E., et al. 2024, A&A, 691, A145
Matthee, J., Naidu, R. P., Brammer, G., et al. 2024, ApJ, 963, 129
Morishita, T., Stiavelli, M., Mason, C. A., et al. 2025, arXiv e-prints, arXiv:2508.01372
Naidu, R. P., Matthee, J., Katz, H., et al. 2025, arXiv e-prints, arXiv:2503.16596
Nenkova, M., Sirocky, M. M., Ivezić, Ž., & Elitzur, M. 2008, ApJ, 685, 147
Nikopoulos, G. P., Watson, D., Sneppen, A., et al. 2025, arXiv e-prints, arXiv:2510.06362
Pacucci, F. & Narayan, R. 2024, ApJ, 976, 96
Paczyński, B. & Wiita, P. J. 1980, A&A, 88, 23
Pandey, A., Czerny, B., Panda, S., et al. 2023, A&A, 680, A102
Pérez-González, P. G., Barro, G., Rieke, G. H., et al. 2024, ApJ, 968, 4
Peterson, B. M. 2006, in Physics of Active Galactic Nuclei at all Scales, ed. D. Alloin, Vol. 693, 77
Pozo Nuñez, F., Haas, M., Ramolla, M., et al. 2014, A&A, 568, A36
Savić, D. V., Hutsemékers, D., & Sluse, D. 2024, A&A, 687, A114
Schindler, J.-T., Hennawi, J. F., Davies, F. B., et al. 2025, Nature Astronomy, 9, 1732
Setton, D. J., Greene, J. E., Spilker, J. S., et al. 2025, ApJ, 991, L10
Sikora, M. 1981, MNRAS, 196, 257
Stalevski, M., Fritz, J., Baes, M., Nakos, T., & Popović, L. Č. 2012, MNRAS, 420, 2756
Sun, W. Q., Naidu, R. P., Matthee, J., et al. 2026, arXiv e-prints, arXiv:2601.20929
Tang, M., Stark, D. P., Plat, A., et al. 2025, arXiv e-prints [arXiv:2505.06359]
Taylor, A. J., Finkelstein, S. L., Kocevski, D. D., et al. 2025, ApJ, 986, 165
Torralba, A., Matthee, J., Pezzulli, G., et al. 2025, arXiv e-prints, arXiv:2510.00103
Torralba, A., Matthee, J., Pezzulli, G., et al. 2026, A&A, 705, A147
Tripodi, R., Bradač, M., D'Eugenio, F., et al. 2025a, ApJ, 994, L6
Tripodi, R., Martis, N., Markov, V., et al. 2025b, Nature Communications, 16, 9830
Wada, K. 2012, ApJ, 758, 66
Wada, K., Nagao, T., Shimizu, T., et al. 2026, ApJ, 998, 60
Wang, B., de Graaff, A., Davies, R. L., et al. 2025, ApJ, 984, 121
Wang, B., Leja, J., Labbe, I., et al. 2026, arXiv e-prints, arXiv:2602.06024
Wang, J.-M., Qiu, J., Du, P., & Ho, L. C. 2014, ApJ, 797, 65
Wu, Q. & Shen, Y. 2022, ApJS, 263, 42
Yan, Z., Inayoshi, K., Chen, K., & Guo, J. 2025, arXiv e-prints, arXiv:2512.11050
Yue, M., Eilers, A.-C., Ananna, T. T., et al. 2024, ApJ, 974, L26
Zhang, L., Stone, J. M., Mullen, P. D., et al. 2025, ApJ, 995, 26
Zucchi, G., Ji, X., Madau, P., et al. 2025, arXiv e-prints, arXiv:2510.10772